Applied Energy 280 (2020) 115907

Contents lists available at ScienceDirect

Applied Energy

journal homepage: www.elsevier.com/locate/apenergy

Experimental optimization of small–scale structure–adjustable radioisotope thermoelectric generators

Kai Liu [a,c], Xiaobin Tang [a,b,*], Yunpeng Liu [a,b], Zhiheng Xu [a,b], Zicheng Yuan [a], Dongxiao Ji [c], Seeram Ramakrishna [c]

[a] Department of Nuclear Science and Technology, Nanjing University of Aeronautics and Astronautics, Nanjing 210016, China
[b] Key Laboratory of Nuclear Technology Application and Radiation Protection in Astronautics, Ministry of Industry and Information Technology, China
[c] Department of Mechanical Engineering, National University of Singapore, 117574, Singapore

HIGHLIGHTS

- Thermoelectric materials were optimized by Taguchi orthogonal method.
- The best figure of merit for P/N thermoelectric materials reached 0.92 and 1.03.
- Two small–scale 3D radioisotope thermoelectric generators were prepared.
- The devices supplied stable and real-time power for the electronic clock.

GRAPHICAL ABSTRACT

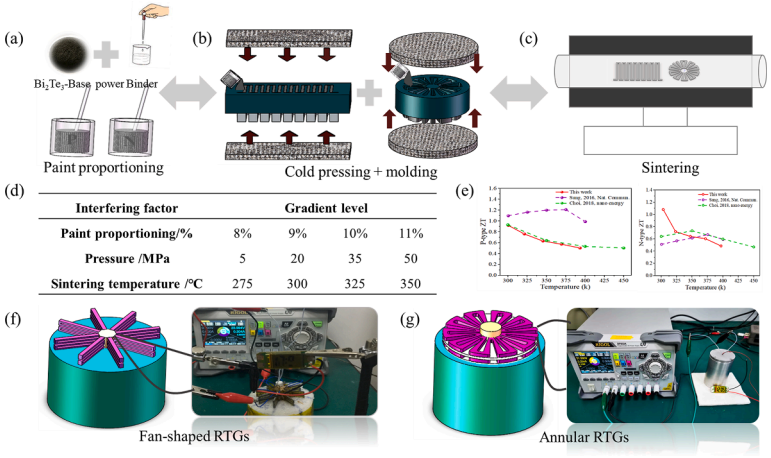

Interfering factor	Gradient level			
Paint proportioning/%	8%	9%	10%	11%
Pressure /MPa	5	20	35	50
Sintering temperature /°C	275	300	325	350

ARTICLE INFO

Keywords:
Cold sintering and molding methods
Radioisotope thermoelectric generator
Taguchi orthogonal method
Space application

ABSTRACT

Small–scale radioisotope thermoelectric generators (RTGs) offer a flexible and scalable power supply for space missions. However, high-performance small-sized RTGs remain challenging. The performance of thermoelectric materials was optimized by Taguchi orthogonal method in this work. Three preparation parameters, including the slurry ratio, cold pressing pressure, and the sintering temperature, along with 4 levels were taken into account. The orthogonal array quickly determined the sensitivity of the performance to the variations of 3 factors. The influences of 3 factors on the *ZT* value were ranked as: cold pressing pressure > slurry ratio > sintering temperature. The optimum operation was 10% paint proportion, 35 MPa pressure, and 598.15 K sintering temperature. Based on this, the optimal *ZT* values of the P/N–type thermoelectric materials reached 0.92 and 1.03 at room temperature, respectively. The principle prototype of the fan–shaped and annular RTGs were well prepared by the cold sintering and molding methods. Those RTGs obtained open–circuit voltages of 1.17 and

* Corresponding author at: Department of Nuclear Science and Technology, Nanjing University of Aeronautics and Astronautics, Nanjing 210016, China.
E-mail address: tangxiaobin@nuaa.edu.cn (X. Tang).

https://doi.org/10.1016/j.apenergy.2020.115907
Received 25 May 2020; Received in revised form 6 September 2020; Accepted 22 September 2020
Available online 10 October 2020

1.56 V, and maximum output powers of 1.9 and 3.39 mW at 398.15 K. These stable and adequate energy is able to directly power for meteorological monitoring equipment, seismometer, and microsatellites.

Nomenclature

C_d	heat capacity at constant volume
d	mean free path of the phonon
L	Lorentz constant
h	Planck constant
K_B	Boltzmann constant
m^*	effective mass
n	carrier concentration, /cm^3
N	number of thermoelectric legs
P_{max}	maximum output power of the RTG, W
P_{out}	output power of the RTG, W
q	carrier charge, C
R	external load resistance in the RTG, Ω
r	internal resistance in the RTG, Ω
S	cross-sectional area of a single P-type or N-type leg, mm^2
V	output voltage of the RTG, V
V_{oc}	open–circuit voltage of the RTG, V
ZT	figure of merit of thermoelectric materials
ΔT	temperature difference of both sides of thermoelectric devices, K
σ	electrical conductivity, S/m
α	Seebeck coefficient, V/K
κ	thermal conductivity, W/(m·K)
κ_L	lattice thermal conductivity, W/(m·K)
κ_e	carrier thermal conductivity, W/(m·K)
ν	diffusion rate of the phonon
μ	carrier mobility, cm^3/(V·s)
ρ	density of thermoelectric materials, g/cm^3

1. Introduction

Space exploration is an emerging and important frontier for humanity. The long–term preparation for space environment monitoring, resource exploration, and space positioning guidance should be investigated thoroughly and strengthened before the formal exploitation. The key challenge is to provide a long–term and continuous power supply for various instruments, including a weather station, accelerometer, and seismometer, in certain regions, such as a planetary surface and deep space [1,2]. At present, solar cells, which are widely used in near–earth orbits and sunlight areas, are still the main power supply in space. However, if a planetary motion or insufficient light in deep space occurs, then solar cells will be unable to provide sufficient power; consequently, the space components will be in a dormant state [3,4]. Storage batteries have a limited amount of service time and exhibit difficulty supplying power to space devices in the long term [5,6]. Radioisotope thermoelectric generators (RTGs), which convert the decay heat of radioisotopes into electrical energy based on the Seebeck effect, have multitudinous merits, namely static energy conversion, compact structure, and long-lifetime, and occupy an irreplaceable position in the space power system [7,8]. Therefore, the RTGs are considered to be ideal power supply devices for deep space exploration, and are developed for miniaturization in response to the requirements of small spacecraft with low–power consumption [9,10].

Compared with the large–scale RTGs owning mature technology, the difficulties in the small–scale RTGs are reflected on not only the small–size preparation of thermoelectric devices, but also the appropriate matching between the thermoelectric devices and the heat sources on the curve surface. Firstly, the preparation of small–size thermoelectric devices should be rightfully considered. The general preparation route of the thermoelectric devices for RTGs is to realize ingot by regional melting and hot pressing synthesis and then assemble small cuboid particles of flat–panel devices through cutting, electroplating, cleaning, and welding steps [11,12]. A large amount of materials and steps are required in the entire process, thereby resulting in expensive cost, time–consuming, and poor matching for the flat–type devices. The production difficulty increases geometrically when the size of the thermoelectric device is as small as several centimeters. Jet Propulsion Laboratory applied fine cutting and welding methods to overcome the production difficulty, and developed a series of small thermoelectric devices of 40–100 mW for RTGs to power Mars science stations for long–term star weather monitoring [13,14]. Secondly, the concern lies in the matching between thermoelectric devices and heat sources. When the RTGs are miniaturized, the thermoelectric device is difficult to match well with the small and curved heat sources. Chen et al. [15,16] prepared segmented flat–panel devices with an efficiency of up to 12% under a temperature difference of 541 K. Obviously, the solid surface of the thermoelectric devices fail to be applied to the curve surface. Some flexible thermoelectric devices are made up of bulk particles and flexible electrodes, and it is a pity that the low–temperature difference and electrical output are still constraints [17,18]. Although thermoelectric devices have many preparation methods, such as chemical vapor deposition [19,20], screen printing [21,22], and 3D printing [23,24], few methods are really suitable for small–scale RTGs with high performance.

Based on the above–mentioned problems, this work optimized the performance of thermoelectric materials for RTGs by Taguchi orthogonal method and prepared small–scale structure–adjustable RTGs by the cold sintering and molding methods. Three preparation parameters along with 4 levels were considered to determine the sensitivity of the performance. The prepared fan–shaped and annular RTGs with volt-level voltage and milliwatt-level power is able to directly power for space components.

2. Small–sized fabrication and optimization scheme

2.1. Small–scale fabrication

The RTGs with diverse structures were manufactured by cold sintering and molding methods [25]. First, the optimal preparation scheme of the thermoelectric materials was determined. The P/N–type Bi_2Te_3–based powder was evenly mixed with binder DER736 in the proportion of 8%–11%, and then the P/N–type painting was filled into the designated position in the mold. Next, the filled mold was pressed within the range of 5–50 MPa pressure. The molded thermoelectric sample was subsequently sintered for 3 h at the temperature range of 548.15–623.15 K. Third, the device was sealed with the polydimethylsiloxane glue to enhance its resistance to vibration and shock. Both ends of electrodes were electroplated with the Ni–Sn layer for the subsequent series connection. Finally, a cylindrical electric heating rod located at the center of the RTG was equivalent to a ^{238}Pu radioisotope heat source to provide the surface temperature range of 323.15–398.15 K [26]. Several arrayed or annular thermoelectric devices were

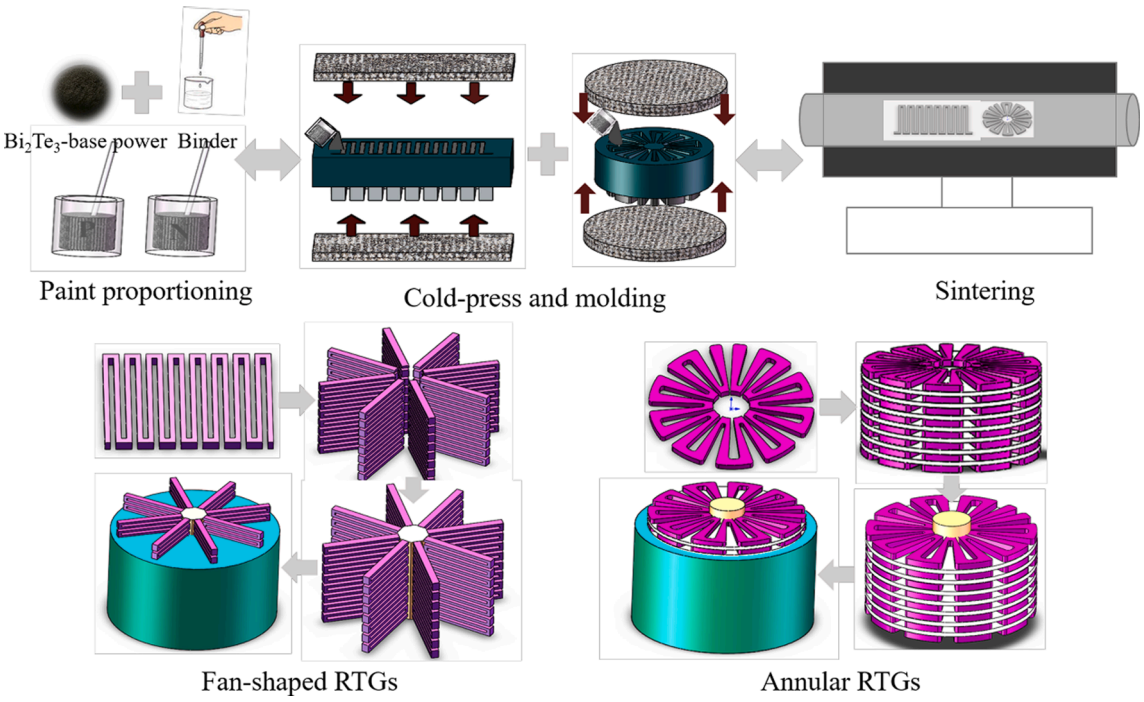

Fig. 1. Preparation process of fan–shaped and annular RTGs.

Table 1
Gradient design of the preparation process parameters.

Interfering factor	Gradient level			
Paint proportion (%)	8	9	10	11
Pressure (MPa)	5	20	35	50
Sintering temperature (K)	548.15	573.15	598.15	623.15

vertically arranged or stacked around the heat source and connected in series according to the structural characteristics of the devices. These devices were placed together in the metal box for encapsulation protection. The gap part was filled with an Al_2O_3 insulation cotton to reduce heat loss (Fig. 1). In this work, the one-time forming of devices with low–aspect ratio, high integration, and variable structure is realized, which is difficult to be realized in the existing preparation methods of thermoelectric devices. It overcomes several difficulties, such as complicated processing problems, high breakage rate, and small temperature difference. The fan–shaped and annular structures are used to realize the fast transmission of heat from the curved surface to the thermoelectric devices, thereby greatly enhancing the engaged preparation effects.

2.2. Optimization scheme based on Taguchi orthogonal method

The preparation process of the small–scale RTGs involves many factors, such as the paint proportion, pressing pressure, and sintering temperature. These preparation processes affect the electrical conductivity, thermal conductivity, and others by intrinsically changing the carrier and phonon transport, and finally boost the electrical performance of the RTGs. Therefore, optimization research on these factors is important and necessary to be effectively conducted [27,28]. (See Table 1.).

$$\alpha = \frac{8\pi K_B^2}{3eh^2} m^* \left(\frac{\pi}{3n}\right)^{\frac{2}{3}} T \tag{1}$$

$$\sigma = ne\mu \tag{2}$$

Table 2
Three–factor four–level orthogonal table based on Taguchi orthogonal method.

Number	Interfering factor		
	Paint proportion (%)	Pressure (MPa)	Sintering temperature (K)
1	8	5	548.15
2	8	20	573.15
3	8	35	598.15
4	8	50	623.15
5	9	5	573.15
6	9	20	548.15
7	9	35	623.15
8	9	50	598.15
9	10	5	598.15
10	10	20	623.15
11	10	35	548.15
12	10	50	573.15
13	11	5	623.15
14	11	20	598.15
15	11	35	573.15
16	11	50	548.15

$$\kappa = \kappa_L + \kappa_e = \frac{C_v \nu d}{3} + L\sigma T \tag{3}$$

$$ZT = \frac{\alpha^2 \sigma}{\kappa} T \tag{4}$$

The paint proportion of the thermoelectric materials, pressing pressure and sintering temperature was regarded as the research objects. A three–factor four–level orthogonal table (Table 2) was designed by using the Taguchi orthogonal method. Then, 16 groups of experimental schemes were performed. The S/N ratio was introduced as a criterion for judging the performance of the thermoelectric materials [29]. The three parameters, namely, power factor ($\alpha^2\sigma$), thermal conductivity (κ), and ZT value, were comprehensively considered to optimize the preparation scheme.

$$S/N = 10\log\frac{1}{n}\sum y_i^2 \tag{5}$$

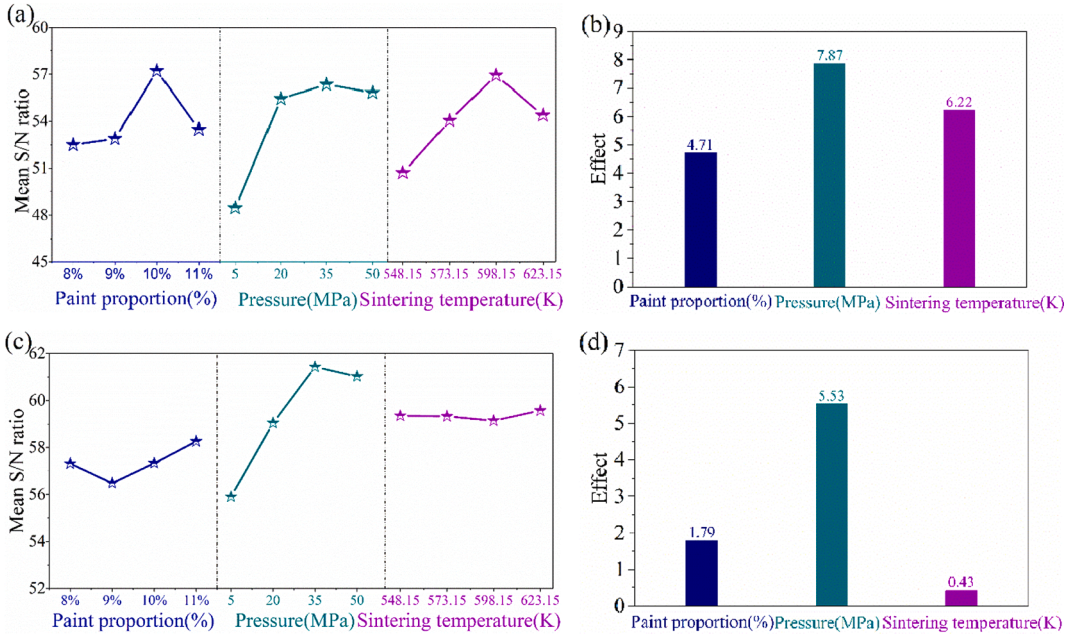

Fig. 2. (a,c) S/N main effect and (b,d) factor effect of P–type $Bi_{0.5}Sb_{1.5}Te_3$,and N–type $Bi_2Se_{0.3}Te_{2.7}$ under different schemes, respectively.

$$S/N = -10\log\frac{1}{n}\sum y_i^2 \tag{6}$$

2.3. Performance testing

With regard to 16 groups of experimental schemes, the Seebeck coefficient/electrical conductivity and thermal conductivity of thermoelectric materials at 348.15 K, simply representing the average value in the range of 298.15–398.15 K, were tested by using thermoelectric effect system (CTA–3) and thermal conductivity tester (DRL–3). When the power or temperature of the heat sources was stable, the internal relation between the electrical outputs of the thermoelectric devices, such as V_{oc} and the output power (P_{out}), and the parameters of the materials were established. The specific calculation equations are as follows [10,11].

$$V_{oc} = (\alpha_p - \alpha_n) \times \Delta T \times N \tag{7}$$

$$P_{out} = \frac{V^2}{(R+r)^2} \times R = \frac{((\alpha_p - \alpha_n)\cdot\Delta T\cdot N)^2}{(R+\frac{\rho l}{S})^2} \times R \tag{8}$$

where N indicates the number of thermocouples; α_p and α_n are the Seebeck coefficients of the P– and N–type thermoelectric materials, respectively; and R is the external resistance of the RTGs. The internal resistance of RTGs (r) is intrinsically related to the size of the thermoelectric legs. The maximum output power (P_{max}) is obtained as $R = r$.

After the optimal preparation scheme was determined, the P/N–type thermoelectric materials and the RTGs were prepared and then tested with a parameter analyzer (Keithley 4200 SCS) at 293.15 K ambient temperature. The electrical heating source provided a constant heat in the range of 323.15–398.15 K. The real–time temperatures of the hot and cold sides of the RTGs were measured with a temperature sensor (R7100). The tests of RTGs at each temperature were conducted after heating them for half an hour to minimize the error in measurement.

3. Scheme determination and material properties

The performance evaluation of thermoelectric devices can be reflected by the thermoelectric parameters of materials. The power factor, thermal conductivity, and ZT value reflect the performance of thermoelectric materials in electricity, thermodynamics, and coupled physics fields, respectively. Taking these three parameters as the evaluation criterion will help to understand the influence of preparation parameters on the thermoelectric performance from many aspects, and then select the optimal scheme.

3.1. Power factor as the evaluation criterion

The power factor reflects the performance of the carrier transport in the material interior. Taking the power factor as the main goal of the thermoelectric performance, the materials prepared by 16 schemes were analyzed by Eq. (5). The result analysis is shown in Fig. 2. Fig. 2(a, c) show the main effect diagram of S/N ratio of the power factor of the P/N thermoelectric materials, including the paint proportion, pressure, and sintering temperature at four levels. Fig. 2(b, d) demonstrate the difference between the maximum and minimum S/N ratios of the three factors at four levels. The comparative analysis shows that the sequence of factors affecting the power factor of the P–type thermoelectric materials is pressure > sintering temperature > paint sintering, thereby reflecting the influencing level of each factor on the power factor of the material, and guiding for the preparation of the actual materials. The combination of the optimal factor level for P–type materials is 10% paint proportion, 35 MPa pressure, and 598.15 K sintering temperature. The sequence of the factors affecting the power factor of the N–type thermoelectric materials is pressure > paint proportion > sintering temperature, where the optimal combination of factor level of N–type materials is 11% paint proportion, 35 MPa pressure, and 623.15 K sintering temperature.

The different sequence between the P–type and N–type factors are attributed to the Seebeck coefficient or electrical conductivity that dominates the differentiated share to power factor in the P/N–type materials. Indeed, the Seebeck coefficient's contribution to the power factor occupies a dominant position, thereby leading to the consistent sequence of factors of power factor. However, the contribution of the electrical conductivity to the power factor is large in the N–type materials, which result in the sequence of power factors consistent with it. The corresponding analysis of Seebeck coefficient and electrical conductivity are shown in Supplementary material. The cold pressure greatly affects the power factor of the P/N–type thermoelectric materials. This situation is because of the role of the pressure that is reflected

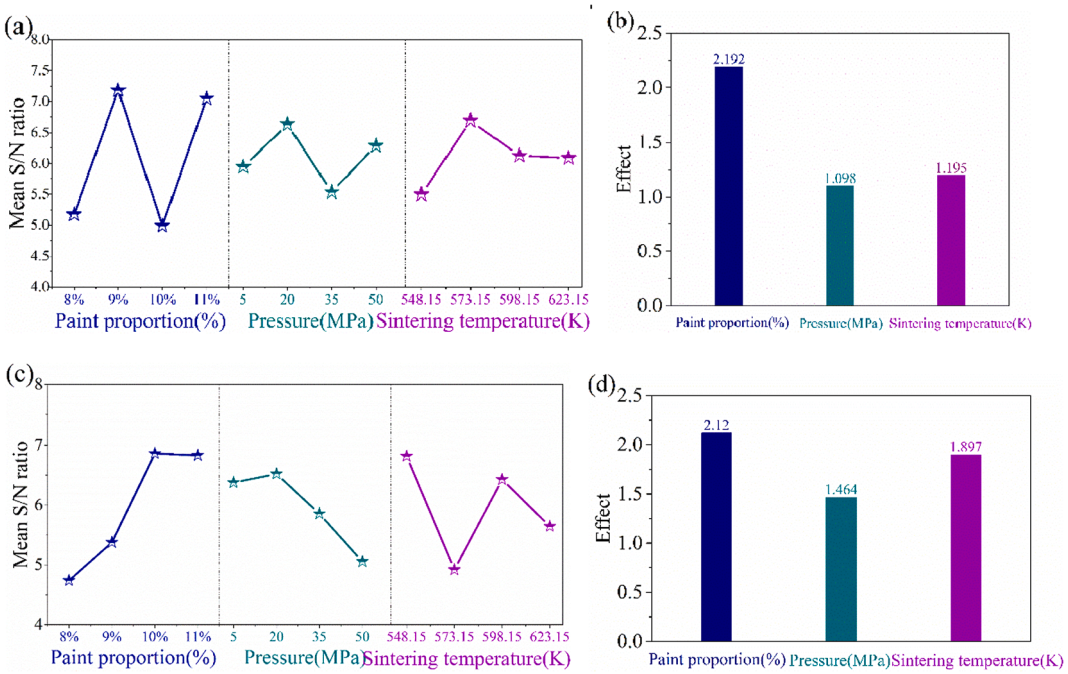

Fig. 3. (a,c) S/N main effect and (b,d) factor effect of P–type $Bi_{0.5}Sb_{1.5}Te_3$ and N–type $Bi_2Se_{0.3}Te_{2.7}$ under different schemes, respectively.

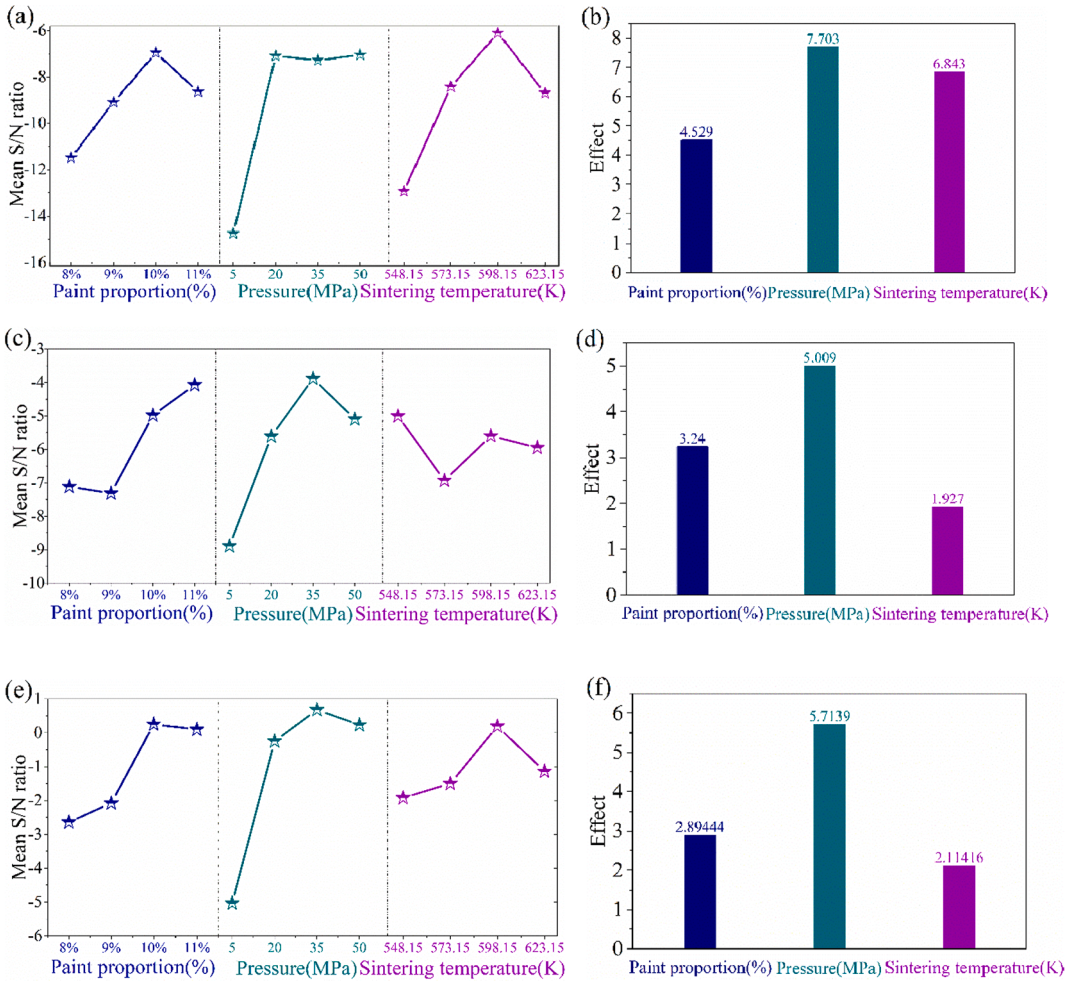

Fig. 4. (a,c, and e) S/N main effect and (b,d, and f) factor effect of P–type $Bi_{0.5}Sb_{1.5}Te_3$, N–type $Bi_2Se_{0.3}Te_{2.7}$, and thermoelectric devices under different schemes, respectively.

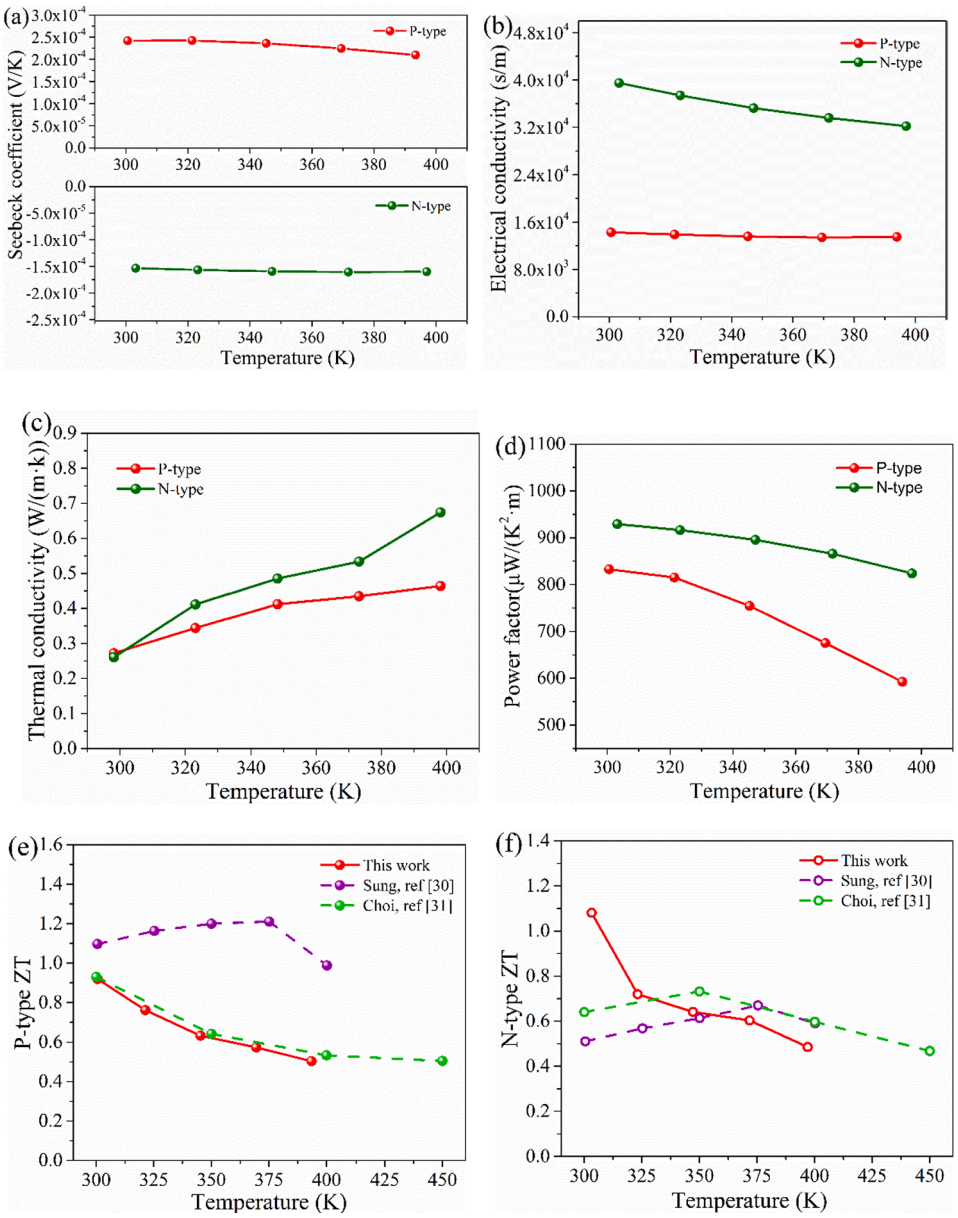

Fig. 5. Thermoelectric properties of the P/N–type thermoelectric materials optimized by the Taguchi orthogonal method. (a) Seebeck coefficient, (b) electrical conductivity, (c) thermal conductivity, (d) power factor, (e) *ZT* of the P–type in comparison with the previously reported Bi_2Te_3–based paints, and (f) *ZT* of the N–type in comparison with previously reported Bi_2Te_3–based paints.

on two aspects. First, the materials are crushed from the loose state to the destruction of the arch bridge effect, resulting in a decrease in the pore volume between the powders. Subsequently, the materials tightly contact each other. Then, a part of the binder is squeezed out by the pressure, indirectly changing the actual paint proportion between the thermoelectric powder and the binder.

3.2. Thermal conductivity as the evaluation criterion

A low thermal conductivity of the material largely helps the thermoelectric device to acquire a great temperature difference between the two ends, thereby macroscopically increasing the V_{oc} of the RTGs. Taking thermal conductivity as the evaluation standard of thermoelectric performance, the materials prepared by 16 schemes were analyzed by Eq. (6). The results are shown in Fig. 3. Fig. 3(a, c) show the main effect diagram of S/N ratios about the thermal conductivity of the P/N–type thermoelectric materials. Fig. 3(b, d) are the differences between the maximum and minimum S/N ratio of three factors at different levels. The sequences of factors determining the thermal conductivity of the P and N–type thermoelectric materials, paint proportion > sintering temperature > cold pressing pressure, are completely consistent. The optimal combination of the factor level for P–type materials is 9% paint proportion, 20 MPa pressure, and 573.15 K sintering temperature, while that for the N–type materials is 10% paint proportion, 20 MPa pressure, and 548.15 K sintering temperature.

The paint proportion, as the most important influencing factor of thermal conductivity, directly reflects the density of the binder molecules around the powder grains. The thermal conductivity of the Der736 binder is low owing to the properties of its epoxy resin, and its ratio with powder directly further affects the thermal conductivity of the final composite thermoelectric material. As much binder content as possible will reduce the thermal conductivity of the material. However, the molecular ratio of the thermoelectric paint changes after cold pressing (the second influencing factor) due to the wettability difference between

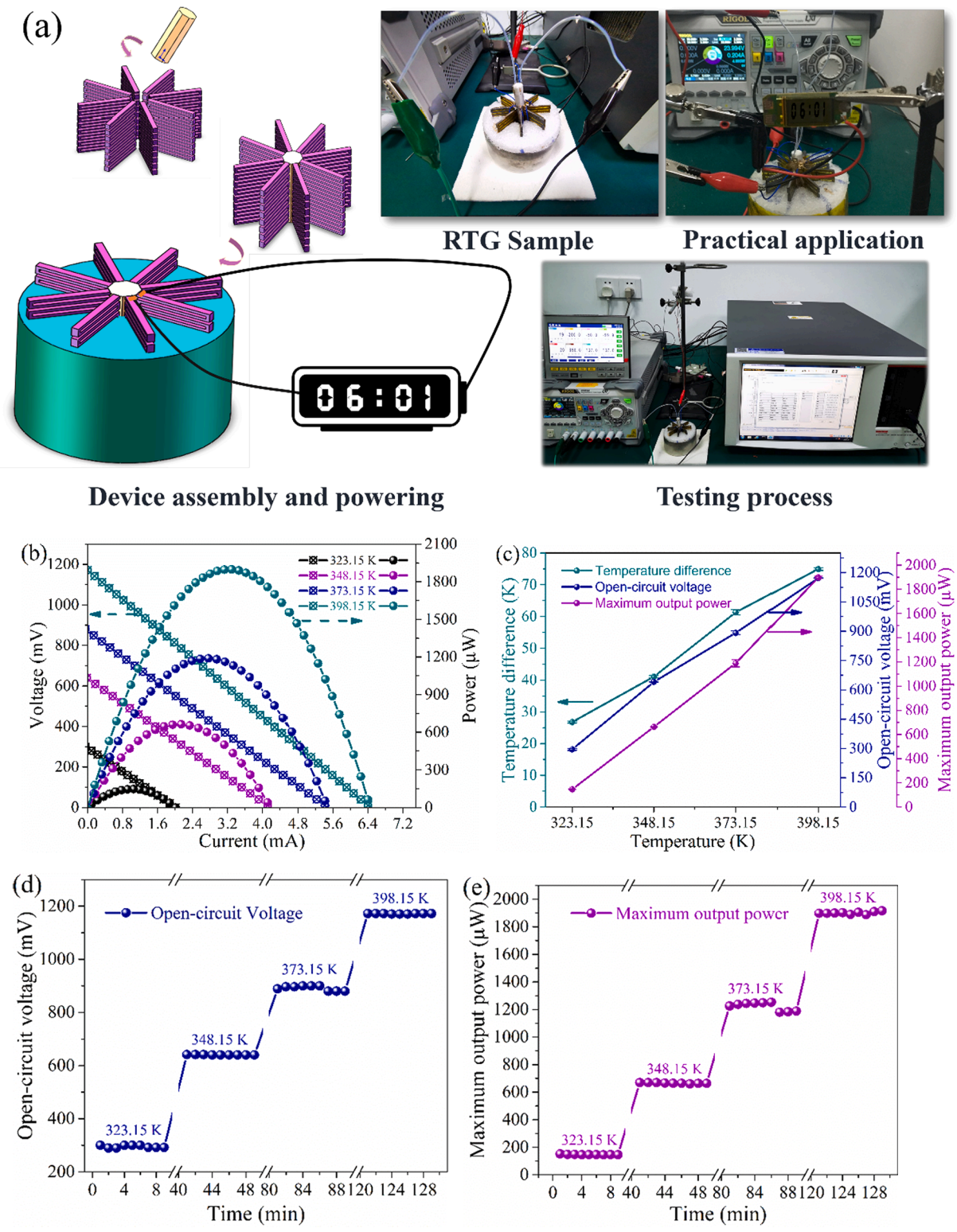

Fig. 6. Electrical performance of the fan–shaped RTGs. (a) Structural design and power supply display, (b,c) *V–I/P–I* curve, (d,e) fluctuation curve between V_{oc} and P_{max} with time.

the powder and the binder for P/N–type materials. Consequently, the two optimal paint proportion of the P/N–type becomes inconsistent. Part of Der736 in the composite thermoelectric material is volatilized after sintering, and the remaining position forms a cavity inside the material, thereby decreasing the thermal conductivity of the material to a certain extent.

3.3. *ZT* value as the evaluation criterion

The performance of thermoelectric materials should be comprehensively evaluated via the *ZT* value. The materials prepared by 16 schemes were analyzed by Eq. (5) when the *ZT* value was considered to be the judging criterion of the material performance. Fig. 4(a, c) show the main effect diagram of the S/N ratios of the *ZT* value of P/N thermoelectric

Table 3
Related dimensions of the fan–shaped RTGs.

Type	Size (mm)	Description
Heat source	Φ8 × 70	Equivalent surface temperature of 323.15–398.15 K
Thermoelectric leg	20 × 1 × 1.6	8 pairs (16 legs)
Thermoelectric module	31 × 21 × 1.6	8 modules
Whole RTG	Φ50 × 78	——

materials. Fig. 4(b, d) are the differences between the maximum and minimum S/N ratios of the three factors at different levels. The factor sequence affecting the *ZT* value of the P–type thermoelectric materials is pressure > sintering temperature > paint proportion. The optimal factor level combination is 10% paint proportion, 50 MPa pressure, and 598.15 K sintering temperature. Meanwhile, the factor sequence of the N–type thermoelectric materials is pressure > paint proportioning > sintering temperature, where its optimal factor level combination is 11% paint proportion, 35 MPa pressure, and 548.15 K sintering temperature. The factor sequence of the P/N–type thermoelectric materials is consistent with that of their power factors. This finding indicates that this optimization helps improve the *ZT* value of the material by adjusting the power factor from the Seebeck coefficient or electrical conductivity.

The P/N–type thermoelectric legs should have the same manufacturing process, considering the one–time forming process of the thermoelectric device based on the cold sintering and molding methods. Given that the P/N–type thermoelectric legs have the identical size and temperature conditions, ZT_{total} ($=ZT_P + ZT_N$) is introduced to characterize the *ZT* value of the thermoelectric device. This study analyzed the S/N ratio of ZT_{total} with Eq. (5), and the obtained factor sequence of the optimal device is pressure > paint proportion > sintering temperature, in which the optimal factor combination is 10% paint proportion, 35 MPa pressure, and 598.15 K sintering temperature. This result is highly rigorous and reasonable to develop high–performance thermoelectric materials and devices.

3.4. Thermoelectric performance of the P/N–type materials

The P/N–type thermoelectric paint was prepared with an optimal combination of 10% paint proportion, 35 MPa pressure, and 598.15 K sintering temperature for 210 min. Thereafter, the thermoelectric properties of the prepared materials were characterized (Fig. 5). The prepared P–type thermoelectric material exhibited good Seebeck coefficients in the low temperature range of 298.15–398.18 K, and changed in the range of 210–242 μV/K. In contrast with the P–type material, the N–type one demonstrated better electrical conductivity in the corresponding temperature, thereby reaching 3.22×10^4–3.95×10^4 S·m. The thermal conductivity of the P/N–type thermoelectric material tested in the low temperature range did not exceed 0.46 and 0.67 W/(m•K) at 398.15 K. After the optimization of the preparation process, the *ZT* value of the P– and N–type thermoelectric material were obtained at room temperature, reaching 0.92 and 1.03, respectively. More significantly, the two P and N–type thermoelectric materials with excellent performance were simultaneously obtained under the one–time operation, and each one was competitive in the work of existing Bi_2Te_3–based inorganic thermoelectric paints [30,31]. The Taguchi orthogonal method was used to design the process of cold sintering and molding methods, and excellent thermoelectric materials were rapidly and effectively obtained in this part, which guides on the preparation and optimization of thermoelectric paint, and provides a material basis with excellent performance for the next step of device preparation.

4. Proof–of–concept small–scale RTGs

4.1. Fan–shaped RTGs

Aiming at the application characteristics of the arrayed thermoelectric devices, the fan–shaped small–scale RTG was systematically prepared to achieve a nice match between the thermoelectric device and the heat source (Fig. 6(a)). Eight thermoelectric devices were in contact with the heat source through a plurality of narrow cross–section of thermoelectric legs, thereby achieving a centralized and rapid heat transfer. The specific dimensions are shown in Table 3. The electrical performances of the fan–shaped small–scale RTGs were measured by controlling the surface temperature of the heat source in the range of 323.15–398.15 K.

The internal resistance of the RTG was 146.63 Ω at room temperature. When the temperature of the heat source was 398.15 K, the temperature difference between the two ends of the device increased to 74.9 K. Accordingly, a good heat transfer of the contact surfaces and low thermal conductivity of the material were obtained. The V_{oc} of the RTG reached 1.17 V, and the P_{max} reached 1.9 mW. The electrical output of the RTG was always stable under the temperature range of the heat source. During the 398.15 K interval, the maximum fluctuation of the V_{oc} did not exceed 0.12%, while that of P_{max} never exceeded 0.8%. In order to verify the feasibility of actual power supplies for small devices, the prepared RTG was directly connected to the electronic clock to demonstrate the capabilities of this practical application. The association of the 1.17 V V_{oc} and the 1.9 mW P_{max} provided by the RTG successfully achieved the normal timing of the electronic clock, and the electronic clock has been constantly working. It was commendable that there is no other circuit of voltage regulation or energy storage involved, which shows the feasibility of providing sufficient power for space electronic components.

4.2. Annular RTGs

For the sake of enhancing the space utilization and increase the heat transfer between the heat source and the thermoelectric devices, an annular radial RTGs were designed and prepared. As shown in Fig. 7(a), the annular thermoelectric devices possess a hollow ring to match well with the curve surface of the heat source. The small–scale RTG is made up of stacked eight–layer devices in series. The specific dimensions are shown in Table 4. The electrical performance output of the RTG was tested for the 323.15–398.15 K temperature of the heat source.

The internal resistance of the RTG was 156.3 Ω at room temperature when the heat source was unloaded. As the temperature of the heat source increased to 398.15 K, the temperature difference across the device increased, reaching a maximum of 64.3 K. The high performance of V_{oc} (1.56 V) of and P_{max} (3.93 mW) was simultaneously achieved. The electrical output of RTGs keeps little fluctuation during each of the heat source temperatures in Fig. 7(d, e). The maximum fluctuations of V_{oc} and P_{max} within the 398.15 K interval did not exceed 0.67% and 0.35%, respectively. The application ability of the annular RTGs was more powerful than that of the fan–shaped one mainly due to the reasonable matching of the annular design and multiple P/N–type thermoelectric legs. The RTG was directly connected to the electronic clock in Fig. 7(a). The concurrency of high V_{oc} and P_{max} at 398.15 K easily achieved the normal timing of the electronic clock without any other electronic conversion circuit, efficiently balancing the relationship between power and voltage in the RTGs. (video in the Supplementary material). Such electrical output at this voltage and milliwatt level could be capable of satisfying most power demand of small space components. Thereupon, the application potential is predictably huge for the long–term space tasks, such as scientific equipment and microsatellite. Further increase of the power output of the RTGs for electronic components in diverse occasions is possible through the numerous thermoelectric devices connected in series or a large–scale design.

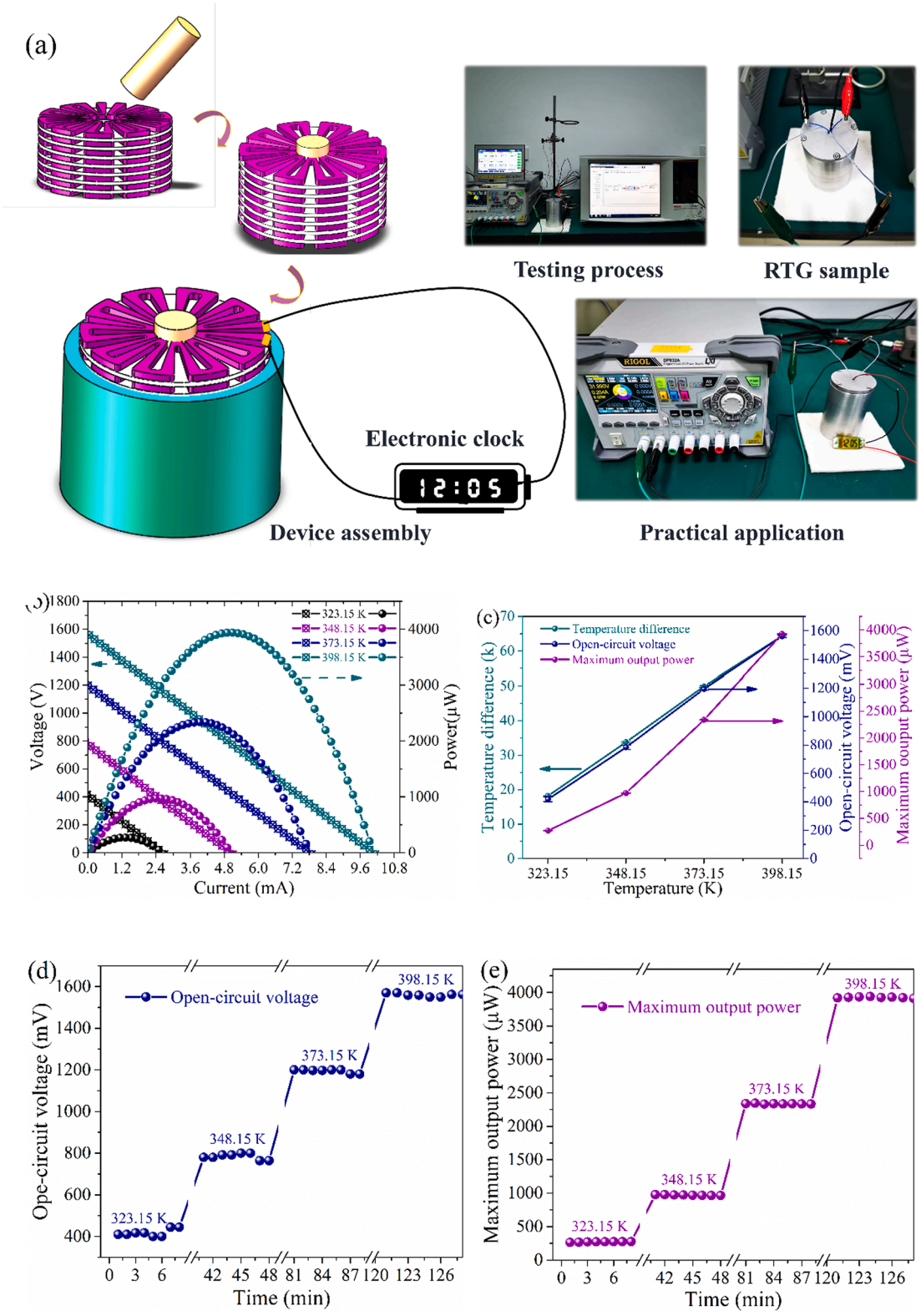

Fig. 7. Electrical performance of the annular RTGs. (a) Structural design and power supply display, (b, c) *V–I*/*P–I* curve, (d, e) fluctuation curve between V_{oc} and P_{max} with time.

5. Conclusions

The thermoelectric performance of 3D small-scale structure-adjustable radioisotope thermoelectric generators has been investigated by means of the Taguchi orthogonal method. Three preparation parameters (i.e., the slurry ratio and cold pressing pressure as well as the sintering temperature) along with 4 levels were considered. A $L_{16}(3^4)$ orthogonal array was built to figure out the sensitivity of the performance to the variations of 3 factors. The *ZT* value was used as the final indicators. The analysis suggested that the influences of the 3 factors on the *ZT* value are

Table 4
Related dimensions of annular RTGs.

Type	Size (mm)	Description
Heat source	Φ8 × 70	Equivalent surface temperature of 323.15–398.15 K
Thermoelectric leg	15.5×(0.7–3.14) × 1.5	10 pairs (20 legs)
Thermoelectric module	Φ9/Φ40 × 70	8 modules
Whole RTG	Φ45 × 78	——

ranked as: cold pressing pressure > slurry ratio > sintering temperature, and their values for optimum operation are 10% paint proportion, 35 MPa pressure, and 598.15 K sintering temperature. This reflects that the cold pressing pressure is the most important factor in determining the performance of the thermoelectric materials for RTGs. Therefore, the optimal *ZT* values of the P/N–type thermoelectric materials reached 0.92 and 1.03 at room temperature, respectively. Thus, the thermoelectric materials with excellent performance for RTG were obtained by Taguchi orthogonal method. Based on above optimized thermoelectric materials, two small–scale RTGs for aerospace application were synthesized by the cold sintering and molding methods. The fan–shaped and annular small–scale RTGs obtained V_{oc} of 1.17 V and 1.56 V, and P_{max} of 1.9 mW and 3.93 mW at 398.15 K, respectively. The energy curve about time showed that it can provide stable and real–time volt–level voltage and milliwatt–level power for the electronic clock. In the case of solving the existing preparation problems, the prepared RTGs are capable of powering for the meteorological monitoring equipment, seismometers, and microsatellites in space. In the future, high-quality electrode series and large-size design will further harvest energy.

CRediT authorship contribution statement

Kai Liu: Conceptualization, Methodology, Writing - original draft. **Xiaobin Tang:** Conceptualization, Writing - review & editing. **Yunpeng Liu:** Validation, Writing - review & editing. **Zhiheng Xu:** Formal analysis, Writing - review & editing. **Zicheng Yuan:** Visualization, Writing - review & editing. **Dongxiao Ji:** Methodology, Writing - review & editing. **Seeram Ramakrishna:** Methodology, Writing - review & editing.

Declaration of Competing Interest

The authors declare that they have no known competing financial interests or personal relationships that could have appeared to influence the work reported in this paper.

Acknowledgements

This work was supported by the Fundamental Research Funds for the Central Universities (Grant No. NP2018462), the Postgraduate Research & Practice Innovation Program of Jiangsu Province (Grant No. KYCX19_0176), and the Short Visit Program of Nanjing University of Aeronautics and Astronautics (Grant No. 191104DF06).

Appendix A. Supplementary data

Supplementary data to this article can be found online at https://doi.org/10.1016/j.apenergy.2020.115907.

References

[1] Simon M, Latorella K, Martin J, Cerro J, Lepsch R, Jefferies S, et al. IEEE Aerosp. Conf. 2017;2017:1–34. https://doi.org/10.1109/AERO.2017.7943662.
[2] Zelenyi LM, Korablev OI, Rodionov DS, Novikov BS, Marchenkov KI, Andreev ON. Scientific objectives of the scientific equipment of the landing platform of the ExoMars–2018 mission. Sol Syst Res 2015;49:509–17. https://doi.org/10.1134/S0038094615070229.
[3] Rauschenbach HS. Solar cell array design handbook: the principles and technology of photovoltaic energy conversion. Springer Science & Business Media; 2012.
[4] Dey GK, Ahmmed KT. Multi–junction solar cells and microwave power transmission technologies for solar power satellite. In: Int Conf Informatics, Electron Vis, 2014. IEEE; 2014. p. 1–6. https://doi.org/10.1109/ICIEV.2014.6850721.
[5] Walker W, Ardebili H. Thermo–electrochemical analysis of lithium ion batteries for space applications using Thermal Desktop. J Power Sources 2014;269:486–97. https://doi.org/10.1016/j.jpowsour.2014.07.020.
[6] Shimizu T, Underwood C. Super–capacitor energy storage for micro–satellites: Feasibility and potential mission applications. Acta Astronaut 2013;85:138–54. https://doi.org/10.1016/j.actaastro.2012.12.005.
[7] Holgate TC, Bennett R, Hammel T, Caillat T, Keyser S, Sievers B. Increasing the efficiency of the multi–mission radioisotope thermoelectric generator. J Electron Mater 2015;44:1814–21. https://doi.org/10.1007/s11664-016-4776-y.
[8] Matthes CSR, Woerner DF, Hendricks TJ, Fleurial J-P, Oxnevad KI, Barklay CD, et al. IEEE Aerosp. Conf. IEEE 2018;2018:1–9. https://doi.org/10.1109/AERO.2018.8396738.
[9] Gusev VV, Pustovalov AA, Rybkin NN, Anatychuk LI, Demchuk BN, Ludchak IY. Milliwatt–power radioisotope thermoelectric generator (RTG) based on plutonium–238. J. Electron. Mater. 2011. https://doi.org/10.1007/s11664-011-1579-z.
[10] Liu K, Tang X, Liu Y, Xu Z, Yuan Z, Li J. Preparation and optimization of miniaturized radioisotope thermoelectric generator based on concentric filament architecture. J Power Sources 2018;407:14–22. https://doi.org/10.1016/j.jpowsour.2018.10.052.
[11] Liu K, Liu Y, Xu Z, Zhang Z, Yuan Z, Guo X, et al. Experimental prototype and simulation optimization of micro–radial milliwatt–power radioisotope thermoelectric generator. Appl Therm Eng 2017. https://doi.org/10.1016/j.applthermaleng.2017.07.022.
[12] Fabián-Mijangos A, Min G, Alvarez-Quintana J. Enhanced performance thermoelectric module having asymmetrical legs. Energy Convers Manag 2017;148:1372–81. https://doi.org/10.1016/j.enconman.2017.06.087.
[13] Allen DT, Bass JC, Elsner NB, Ghamaty S, Morris CC. Milliwatt thermoelectric generator for space applications. Sp Technol Appl Int Forum, Pts 2000;1(2):504. https://doi.org/10.1063/1.1290968.
[14] Drinker RW, Reddy A, Heshmatpour B, Snyder GJ, Tuttle KL. Advanced superlattice BiTe–PbTe/TAGS milliwatt radioisotope power system. AIP Conf Proc 2005. https://doi.org/10.1063/1.1867157.
[15] Zhang Q, Zhou Z, Dylla M, Agne MT, Pei Y, Wang L. Realizing high–performance thermoelectric power generation through grain boundary engineering of skutterudite–based nanocomposites. Nano Energy 2017;41:501–10. https://doi.org/10.1016/j.nanoen.2017.10.003.
[16] Zhang Q, Liao J, Tang Y, Gu M, Ming C, Qiu P. Realizing a thermoelectric conversion efficiency of 12% in bismuth telluride/skutterudite segmented modules through full–parameter optimization and energy–loss minimized integration. Energy Environ Sci 2017;10:956–63. https://doi.org/10.1039/C7EE00447H.
[17] Sargolzaeiaval Y, Ramesh VP, Neumann TV, Misra V, Vashaee D, Dickey MD, et al. Flexible thermoelectric generators for body heat harvesting–Enhanced device performance using high thermal conductivity elastomer encapsulation on liquid metal interconnects. Appl Energy 2020;262:114370. https://doi.org/10.1016/j.apenergy.2019.114370.
[18] Wang Y, Shi Y, Mei D, Chen Z. Wearable thermoelectric generator to harvest body heat for powering a miniaturized accelerometer. Appl Energy 2018;215:690–8. https://doi.org/10.1016/j.apenergy.2018.02.062.
[19] Kim KC, Kwon B, Kim HJ, Baek SH, Bin Hyun D, Kim SK. Sn doping in thermoelectric Bi_2Te_3 films by metal–organic chemical vapor deposition. Appl Surf Sci 2015. https://doi.org/10.1016/j.apsusc.2015.06.106. 353:232–7.
[20] Cecchini R, Gajjela RSR, Martella C, Wiemer C, Lamperti A, Nasi L. High-Density Sb_2Te_3 Nanopillars Arrays by Templated Bottom-Up MOCVD Growth. Small 2019;15:1901743. https://doi.org/10.1002/smll.201901743.
[21] Kim SJ, Choi H, Kim Y, We JH, Shin JS, Lee HE. Post ionized defect engineering of the screen–printed $Bi_2Te_{2.7}Se_{0.3}$ thick film for high performance flexible thermoelectric generator. Nano Energy 2017;31:258–63. https://doi.org/10.1016/j.nanoen.2016.11.034.
[22] Choi H, Kim YJ, Song J, Kim CS, Lee GS, Kim S. UV-Curable Silver Electrode for Screen-Printed Thermoelectric Generator. Adv Funct Mater 2019;29:1901505. https://doi.org/10.1002/adfm.201901505.
[23] Qiu J, Yan Y, Luo T, Tang K, Yao L, Zhang J. 3D Printing of highly textured bulk thermoelectric materials: mechanically robust BiSbTe alloys with superior performance. Energy Environ Sci 2019;12:3106–17. https://doi.org/10.1039/C9EE02044F.
[24] Burton MR, Mehraban S, Beynon D, McGettrick J, Watson T, Lavery NP. 3D printed SnSe thermoelectric generators with high figure of merit. Adv Energy Mater 2019;9:1900201. https://doi.org/10.1002/aenm.201900201.
[25] Guo J, Baker AL, Guo H, Lanagan M, Randall CA. Cold sintering process: a new era for ceramic packaging and microwave device development. J Am Ceram Soc 2017;100:669–77. https://doi.org/10.1111/jace.14603.
[26] Whalen SA, Aplett CA, Aselage TL. Improving power density and efficiency of miniature radioisotopic thermoelectric generators. J Power Sources 2008;180:657–63. https://doi.org/10.1016/j.jpowsour.2008.01.080.
[27] Yang L, Chen Z, Dargusch MS, Zou J. High performance thermoelectric materials: progress and their applications. Adv Energy Mater 2018;8:1701797. https://doi.org/10.1002/aenm.201701797.

[28] Snyder GJ, Toberer ES. Complex thermoelectric materials. Mater. Sustain. energy a Collect. peer-reviewed Res. Rev Artic Nat Publ Gr, World Scientific 2011:101–10. https://doi.org/10.1142/9789814317665_0016.
[29] Chen W-H, Huang S-R, Lin Y-L. Performance analysis and optimum operation of a thermoelectric generator by Taguchi method. Appl Energy 2015;158:44–54. https://doi.org/10.1016/j.apenergy.2015.08.025.
[30] Park SH, Jo S, Kwon B, Kim F, Ban HW, Lee JE. High–performance shape–engineerable thermoelectric painting. Nat Commun 2016;7:1–10. https://doi.org/10.1038/ncomms13403.
[31] Choi H, Kim YJ, Kim CS, Yang HM, Oh MW, Cho BJ. Enhancement of reproducibility and reliability in a high–performance flexible thermoelectric generator using screen–printed materials. Nano Energy 2018;46:39–44. https://doi.org/10.1016/j.nanoen.2018.01.031.